The Astrophysical Journal, 779:150 (10pp), 2013 December 20 doi:10.1088/0004-637X/779/2/150

VERITAS OBSERVATIONS OF THE MICROQUASAR CYGNUS X-3

S. Archambault[1], M. Beilicke[2], W. Benbow[3], K. Berger[4], R. Bird[5], A. Bouvier[6], J. H. Buckley[2], V. Bugaev[2], K. Byrum[7], M. Cerruti[3], X. Chen[8,9], L. Ciupik[10], M. P. Connolly[11], W. Cui[12,33], C. Duke[13], J. Dumm[14], M. Errando[15], A. Falcone[16], S. Federici[8,9], Q. Feng[12], J. P. Finley[12], L. Fortson[14], A. Furniss[6], N. Galante[3], G. H. Gillanders[11], S. Griffin[1], S. T. Griffiths[17], J. Grube[10], G. Gyuk[10], D. Hanna[1], J. Holder[4], G. Hughes[9], T. B. Humensky[18], P. Kaaret[17], M. Kertzman[19], Y. Khassen[5], D. Kieda[20], H. Krawczynski[2], M. J. Lang[11], A. S. Madhavan[21], G. Maier[9], P. Majumdar[22,23], S. McArthur[24], A. McCann[25], P. Moriarty[26], R. Mukherjee[15], D. Nieto[18], A. O'Faoláin de Bhróithe[5], R. A. Ong[22], A. N. Otte[27], D. Pandel[28], N. Park[24], J. S. Perkins[29], M. Pohl[8,9], A. Popkow[22], H. Prokoph[9], J. Quinn[5], K. Ragan[1], J. Rajotte[1], L. C. Reyes[30], P. T. Reynolds[31], G. T. Richards[27], E. Roache[3], G. H. Sembroski[12], F. Sheidaei[20], A. W. Smith[20], D. Staszak[1], I. Telezhinsky[8,9], M. Theiling[12], J. V. Tucci[12], J. Tyler[1], A. Varlotta[12,33], S. Vincent[9], S. P. Wakely[24], T. C. Weekes[3], A. Weinstein[21], D. A. Williams[6], B. Zitzer[7]
(The VERITAS Collaboration)
and
M. L. McCollough[32]
(Smithsonian Astrophysical Observatory)
[1] Physics Department, McGill University, Montreal, QC H3A 2T8, Canada
[2] Department of Physics, Washington University, St. Louis, MO 63130, USA
[3] Fred Lawrence Whipple Observatory, Harvard-Smithsonian Center for Astrophysics, Amado, AZ 85645, USA
[4] Department of Physics and Astronomy and the Bartol Research Institute, University of Delaware, Newark, DE 19716, USA
[5] School of Physics, University College Dublin, Belfield, Dublin 4, Ireland
[6] Santa Cruz Institute for Particle Physics and Department of Physics, University of California, Santa Cruz, CA 95064, USA
[7] Argonne National Laboratory, 9700 S. Cass Avenue, Argonne, IL 60439, USA
[8] Institute of Physics and Astronomy, University of Potsdam, D-14476 Potsdam-Golm, Germany
[9] DESY, Platanenallee 6, D-15738 Zeuthen, Germany
[10] Astronomy Department, Adler Planetarium and Astronomy Museum, Chicago, IL 60605, USA
[11] School of Physics, National University of Ireland Galway, University Road, Galway, Ireland
[12] Department of Physics, Purdue University, West Lafayette, IN 47907, USA; avarlott@purdue.edu, cui@purdue.edu
[13] Department of Physics, Grinnell College, Grinnell, IA 50112-1690, USA
[14] School of Physics and Astronomy, University of Minnesota, Minneapolis, MN 55455, USA
[15] Department of Physics and Astronomy, Barnard College, Columbia University, NY 10027, USA
[16] Department of Astronomy and Astrophysics, 525 Davey Lab, Pennsylvania State University, University Park, PA 16802, USA
[17] Department of Physics and Astronomy, University of Iowa, Van Allen Hall, Iowa City, IA 52242, USA
[18] Physics Department, Columbia University, New York, NY 10027, USA
[19] Department of Physics and Astronomy, DePauw University, Greencastle, IN 46135-0037, USA
[20] Department of Physics and Astronomy, University of Utah, Salt Lake City, UT 84112, USA
[21] Department of Physics and Astronomy, Iowa State University, Ames, IA 50011, USA
[22] Department of Physics and Astronomy, University of California, Los Angeles, CA 90095, USA
[23] Saha Institute of Nuclear Physics, Kolkata 700064, India
[24] Enrico Fermi Institute, University of Chicago, Chicago, IL 60637, USA
[25] Kavli Institute for Cosmological Physics, University of Chicago, Chicago, IL 60637, USA
[26] Department of Life and Physical Sciences, Galway-Mayo Institute of Technology, Dublin Road, Galway, Ireland
[27] School of Physics and Center for Relativistic Astrophysics, Georgia Institute of Technology, 837 State Street NW, Atlanta, GA 30332-0430, USA
[28] Department of Physics, Grand Valley State University, Allendale, MI 49401, USA
[29] NASA/Goddard Space Flight Center, Code 661, Greenbelt, MD 20771, USA
[30] Physics Department, California Polytechnic State University, San Luis Obispo, CA 94307, USA
[31] Department of Applied Physics and Instrumentation, Cork Institute of Technology, Bishopstown, Cork, Ireland
[32] Smithsonian Astrophysical Observatory, 60 Garden Street, Cambridge, MA 02138, USA
Received 2013 July 22; accepted 2013 October 28; published 2013 December 3

ABSTRACT

We report results from TeV gamma-ray observations of the microquasar Cygnus X-3. The observations were made with the Very Energetic Radiation Imaging Telescope Array System (VERITAS) over a time period from 2007 June 11 to 2011 November 28. VERITAS is most sensitive to gamma rays at energies between 85 GeV and 30 TeV. The effective exposure time amounts to a total of about 44 hr, with the observations covering six distinct radio/X-ray states of the object. No significant TeV gamma-ray emission was detected in any of the states, nor with all observations combined. The lack of a positive signal, especially in the states where GeV gamma rays were detected, places constraints on TeV gamma-ray production in Cygnus X-3. We discuss the implications of the results.

Key words: acceleration of particles – binaries: close – gamma rays: stars – X-rays: individual (Cygnus X-3)

Online-only material: color figures

1. INTRODUCTION

Cygnus X-3 was among the first X-ray sources to be discovered in the early days of X-ray astronomy. It lies in the Galactic plane, at a distance between 7 kpc and 10 kpc (Predehl et al. 2000; Ling et al. 2009). It is a high-mass X-ray binary, with the companion star appearing to show the spectral characteristics of a Wolf–Rayet star (van Kerkwijk et al. 1996). The nature of the compact object is still being debated. Cygnus X-3 is known to produce intense radio flares, making it at times one of the brightest transient Galactic radio sources. The radio flares can last from a few days to several weeks. Relativistic jets have been seen during major flares ($S_\nu > 10$ Jy at 15 GHz; Mioduszewski et al. 2001; Miller-Jones et al. 2004), with an inclination to the line of sight of $\lesssim 14^\circ$. This makes Cygnus X-3 analogous to the extragalactic blazars, which constitute a major population of known TeV gamma-ray emitters. With an orbital period of only 4.8 hr, the compact object is thought to be enshrouded in the wind of the Wolf–Rayet star.

Cygnus X-3 has long been a prominent target for gamma-ray observations. Initially, there was contradictory evidence for gamma-ray emission at GeV energies: SAS-2 found a periodic signal (Lamb et al. 1977), while COS-B could not confirm it (Bennett et al. 1977). Then, numerous claims of detection of Cygnus X-3 were made in the early days of ground-based gamma-ray experiments, spanning the TeV to PeV energy range (see discussions by Weekes 1992 and Ong 1998). The claims were subsequently disputed by a critical analysis of the observations (Chardin & Gerbier 1989). In subsequent years, Cygnus X-3 was observed with more sensitive ground-based instruments, including Whipple (O'Flaherty et al. 1992), CASA-MIA (Borione et al. 1997), HEGRA (Schilling et al. 2001), and MAGIC (Aleksić et al. 2010), but was not detected. At GeV energies, EGRET/*CGRO* found a gamma-ray source (2EG J2033+4112) that is consistent with the position of Cygnus X-3 (although the position error circle is quite large), but with no evidence for orbital modulation (Mori et al. 1997). The source has now been detected at GeV energies, with high confidence, independently with *AGILE* (Tavani et al. 2009) and *Fermi* LAT (Abdo et al. 2009). Moreover, the orbital modulation of the gamma-ray emission has also been seen (Abdo et al. 2009).

In X-ray binaries, gamma rays may be produced by Compton upscattering of photons, from either the companion star or the accretion disk or both, by relativistic electrons accelerated in the jets of a stellar-mass black hole or in the shocked wind of a pulsar. Detailed models have been constructed for gamma-ray production and attenuation in the jets. In the case of Cygnus X-3, the close proximity ($R_d \approx 3 \times 10^{11}$ cm), high temperature ($T_* \sim 10^5$ K), and high luminosity ($L_* \sim 10^{39}$ erg s^{-1}) of the Wolf–Rayet star may result in the efficient Compton upscattering of stellar photons to produce gamma rays, as well as in the attenuation of the gamma rays via $\gamma\gamma$ pair production (Bednarek 2010). Whether Cygnus X-3 appears as a TeV gamma-ray emitter would depend on the competition between the production and attenuation processes. Theoretically, certain circumstances would favor TeV emission. These typically involve emitting regions at large perpendicular distances ($H \gtrsim 10\, R_d$) from the orbital plane and orbital phases around the inferior conjunction (Bednarek 2010). At lower (GeV) energies, the attenuation optical depth is much reduced, so the observed orbital modulation may be mainly associated with the production process (Dubus et al. 2010; Bednarek 2010). Alternatively, gamma rays may also be produced by the decay of π^0 particles, which result from the $p\,p$ collisions between the relativistic protons in the jets and the cold protons of the dense anisotropic stellar wind of the Wolf–Rayet star (Romero et al. 2003).

Cygnus X-3 is a persistent radio source. Its radio flux may vary by four orders of magnitude. Based on the long-term monitoring of the source with the Green Bank Interferometer, four radio states were identified (Waltman et al. 1994): quiescent state (60–140 mJy), minor flaring state ($\lesssim$1 Jy), quenched state ($\lesssim$30 mJy), and intermediate/major flaring state (>1 Jy). The major flaring state seems to follow the quenched state. The radio emission was subsequently found to be correlated with the hard X-ray emission (McCollough et al. 1999). The correlation is complex and varies with the state that the source is in: it is negative (anti-correlation) in the quiescent state but turns positive in the major flaring and quenched states. No apparent correlation has been observed in the minor flaring state. The radio emission is also correlated with the soft X-ray emission in certain states (Hjalmarsdotter et al. 2008). This is expected because it is known that the soft and hard X-ray fluxes of Cygnus X-3 are generally (but not always) anti-correlated (Choudhury et al. 2002; Hjalmarsdotter et al. 2008). Based on the correlated radio/X-ray properties of the source, Szostek et al. (2008) refined and expanded the definitions of the states. The new radio/X-ray states are now referred to as the *quiescent*, *minor-flaring*, *suppressed*, *quenched*, *major-flaring*, and *post-flaring* states.

The *AGILE* and *Fermi*-LAT observations have shown that the gamma-ray emission from Cygnus X-3 is not steady but episodic. A careful examination of the gamma-ray activities of the source has revealed that gamma-ray production appears to be associated with transitions into or out of the radio *quenched* state (Koljonen et al. 2010). During a transition, the X-ray spectrum of the source becomes dominated by a soft X-ray component (with only a weak power-law component) as its radio flux goes down. For this reason, these time periods are now also referred to as the hypersoft state (Koljonen et al. 2010). As such, the line between the hypersoft state and *quenched* state is not always very clear in practice. Observationally, the hypersoft state is associated with major radio flares and, sometimes, the formation of jets (Koljonen et al. 2010). The latter might be the site of gamma-ray production. This signifies the importance of the hypersoft state to our understanding of Cygnus X-3 as a gamma-ray emitter. Unfortunately, the hypersoft state is very short in duration (lasting for $\lesssim$4–5 days), compared with other states, so it is often challenging to catch it with sensitive instruments of small field of view (FOV).

In this work, we carried out a systematic search for gamma rays from Cygnus X-3 at TeV energies with the Very Energetic Radiation Imaging Telescope Array System (VERITAS). The availability of the contemporaneous radio/X-ray observations of the source made it possible to extend the search to individual radio/X-ray states, particularly to the hypersoft state.

2. VERITAS OBSERVATIONS

VERITAS is a ground-based gamma-ray telescope array located at the Fred Lawrence Whipple Observatory in southern Arizona in the United States. It consists of four 12 m imaging atmospheric Cerenkov telescopes, each with 499-pixel cameras, designed to detect the faint flashes of Cerenkov light from air showers initiated in the atmosphere by TeV gamma rays or

[33] Authors to whom any correspondence should be addressed.

cosmic rays. VERITAS can detect gamma rays in the energy range from 85 GeV to 30 TeV, with a maximum effective area of approximately 10^5 m^2. The energy resolution is about 15%–25%. At 1 TeV, the angular resolution is better than $0.^\circ1$ for an individual gamma event (68% containment level). The pointing accuracy of VERITAS is $<50''$. VERITAS has an FOV of about $3.^\circ5$ in angular diameter. In the summer of 2009, one of the four telescopes of the array was relocated to a different position, increasing the overall sensitivity of the array by about 30%. After the relocation, VERITAS is capable of detecting sources at the flux level of 1% of the Crab Nebula with a ∼25 hr exposure (Holder et al. 2011).

For this work, we used data from observations conducted between 2007 June 11 and 2011 November 28. The observations were conducted under varying weather and other conditions. The design of VERITAS also allows observations to be conducted under partial moonlight. To mitigate the night sky background fluctuations caused by the moonlight, the triggering threshold is increased in the camera photomultiplier tubes, which leads to a higher energy threshold. The triggering threshold in the photomultiplier tubes sets the first step in event discrimination in the telescope array. We carefully examined the data and included all of the observations that we believe can lead to reliable results. The total exposure time amounts to about 44 hr. More detailed information on the observations is shown in Table 1.

The reduction of VERITAS data consists of multiple steps, including rejection of substandard data, flat fielding, pedestal subtraction, pulse integration, image cleaning, parameterization of events, stereo reconstruction of shower direction and impact parameter, and gamma-ray/cosmic-ray separation. Briefly, the data from each participating telescope are first filtered for bad weather or issues with data acquisition and are then charge integrated, pedestal subtracted, and gain corrected. Each resulting image is cleaned and characterized to derive the moments of the light distributions (Hillas 1985). The images of the same air shower from all participating telescopes are used to reconstruct the direction and impact parameter of the shower (see, e.g., Krawczynski et al. 2006). This step requires characterizable images from three or more telescopes. In addition, to separate the gamma-ray events from the cosmic-ray events, we applied selection criteria (based on the energy and geometry of the events) to the events that survived the previous steps. The post-selection energy threshold is about 220 GeV at a 10° zenith angle and 450 GeV at a 40° zenith angle, which correspond approximately to the lowest and highest zenith angle of our data set, respectively. More details about VERITAS, the calibration procedure, and the analysis technique can be found in Acciari et al. (2008).

The VERITAS observation set was the product of different observation modes: it was composed of wobble-mode data on Cygnus X-3, wobble-mode data taken on the TeV gamma-ray source TeV J2032+4130 (Aharonian et al. 2005), which is ∼30′ from Cygnus X-3, and data from tracking mode on the mid-point position between Cygnus X-3 and TeV J2032+4130. In wobble mode, the telescopes are pointed such that the source is always located at a fixed offset ($0.^\circ5$), alternately to the north, south, east, and west of the camera center, for an unbiased estimation of the FOV background of the source region. In tracking mode, the telescopes were pointed alternatively to the east and west of the mid-point position between Cygnus X-3 and TeV J2032+4130. Due to the mixture of different observing modes, the data analysis used the ring background model (Berge et al. 2007). Briefly, the background estimate is derived for a trial source position from an annulus around the source region, which is dependent on the selection criteria. Due to the different offsets of the ring points with respect to the camera center as compared to the source position, a relative event rate, or *acceptance*, correction needs to be applied to normalize the background rate. Any gamma-ray source in the FOV needs to be excluded from the background estimation as well. In our case, we excluded the pixels pointing at bright stars (with B magnitude less than 6) from the background regions. The nearby known TeV gamma-ray source, TeV J2032+4130, was removed from subsequent analyses, to avoid incorrect estimation of the source and background rates of Cygnus X-3 in the analysis.

The data analysis on Cygnus X-3 was performed with selection-criteria parameters based on the energy and geometry configuration of the gamma-ray initiated air showers and modeled on the Crab Nebula. The selection criteria are optimized for a putative source with either a soft (6.6% Crab at 200 GeV, spectral index: −4), medium (2% Crab at 400 GeV, spectral index: −2.4), or hard (2% Crab at 1 TeV, spectral index: −2.0) spectral index. The selection-criteria parameters tend to be looser for softer sources than for harder ones, to allow less event selection restrictions in the analysis. The acceptance correction was consequently generated over the whole data set for soft, medium, and hard selection criteria and then applied to partial data sets (e.g., for individual states). For data taken with the initial VERITAS telescope array configuration (prior to 2009 August) where telescope 1 (T1) and telescope 4 (T4) were in proximity to one another, all T1 and T4 simultaneous events were removed from analysis if no other telescope (T2 or T3) was triggered.

3. SUPPORTING MULTI-WAVELENGTH OBSERVATIONS

To gain a broadband perspective, we also examined data from observations at longer wavelengths. Particularly relevant to this work are contemporaneous gamma-ray observations of Cygnus X-3 at GeV energies made with the Large Area Telescope (LAT) aboard the *Fermi Gamma-Ray Space Telescope* satellite (Atwood et al. 2009), as well as contemporaneous X-ray and radio observations, which make it possible to characterize the radio/X-ray states of the source.

3.1. Fermi-LAT Observations

In the default survey mode, the LAT scans the sky continuously and covers the whole sky once about every three hours. It is sensitive to gamma rays in the nominal energy range of 0.02–300 GeV. Its on-axis effective area is between 8000 and 9000 cm^2 for energies $\gtrsim$1 GeV. The LAT has a very large FOV (∼2.4 sr) and has an angular resolution of better than $0.^\circ1$ at 1 GeV (for 68% containment). For this work, we used the LAT data taken from 2008 August 5 to 2012 March 13.

The LAT data were processed with the Fermi Science Tools (v9r23p1), following the recommendations on event selection from the Fermi Science Support Center.[34] Briefly, the events that have the highest probability of being gamma rays were selected by means of the Pass 7 V6 (P7_V6) source class event selection cut with the `gtselect` tool. In order to minimize contamination from Earth albedo photons, the time periods when Cygnus X-3 was observed at zenith angles greater than 100° were eliminated from further analysis. The energy range was also limited from 0.1 to 100 GeV.

[34] http://fermi.gsfc.nasa.gov/ssc/data/analysis/scitools/

Table 1
Summary of VERITAS Observations

MJD	Calendar Date	X-Ray State	Observing Time (min)	Elevation Range (deg)	$N_{\rm tel}$
54,262	2007 Jun 11	Minor flaring	20	65–69	3
54,263	2007 Jun 12	Minor flaring	40	70–77	3
54,264	2007 Jun 13	Minor flaring	119.5	62–80	3
54,265	2007 Jun 14	Minor flaring	80	72–80	3
54,266	2007 Jun 15	Minor flaring	40	72–78	3
54,626	2008 Jun 9	Quenched	40	76–80	4
54,627	2008 Jun 10	Quenched	40	76–80	4
54,628	2008 Jun 11	Quenched	20	80–81	4
54,731	2008 Sep 22	Suppressed	20	76–78	4
54,774	2008 Nov 4	Quenched	20	59–63	4
54,786	2008 Nov 16	Major flaring	60	59–72	4
54,789	2008 Nov 19	Quenched	60	64–68	4
54,794	2008 Nov 24	Quenched	40	54–60	4
54,800	2008 Nov 30	Quenched	20	54–58	3
54,804	2008 Dec 4	Hypersoft[a]	20	53–56	4
55,126	2009 Oct 22	Quiescent	20	74–76	4
55,127	2009 Oct 23	Quiescent	36	67–74	4
55,128	2009 Oct 24	Quiescent	77	59–79	4
55,129	2009 Oct 25	Quiescent	40	65–74	4
55,155	2009 Nov 20	Quiescent	20	59–62	3
55,156	2009 Nov 21	Quiescent	40	56–64	4
55,157	2009 Nov 22	Quiescent	20	56–59	4
55,158	2009 Nov 23	Quiescent	16	64–67	4
55,382	2010 Jul 5	Minor flaring	20	72–76	4
55,384	2010 Jul 7	Minor flaring	4	80–80	4
55,481	2010 Oct 12	Quiescent	40	75–80	4
55,482	2010 Oct 13	Quiescent	40	69–77	4
55,648	2011 Mar 28	Major flaring	20	42–46	4
55,649	2011 Mar 29	Major flaring	20	42–46	3
55,650	2011 Mar 30	Major flaring	20	43–48	4
55,651	2011 Mar 31	Major flaring	28	45–51	3
55,652	2011 Apr 1	Major flaring	20	42–46	3
55,653	2011 Apr 2	Major flaring	20	42–46	4
55,654	2011 Apr 3	Major flaring	15	48–50	4
55,655	2011 Apr 4	Major flaring	20	48–50	4
55,656	2011 Apr 5	Major flaring	20	48–52	4
55,658	2011 Apr 7	Minor flaring	8	52–53	3
55,659	2011 Apr 8	Minor flaring	23	50–53	4
55,662	2011 Apr 11	Minor flaring	6	55–56	3
55,707	2011 May 26	Minor flaring	20	72–74	4
55,708	2011 May 27	Minor flaring	20	60–64	4
55,709	2011 May 28	Minor flaring	96	65–80	4
55,710	2011 May 29	Minor flaring	52	70–77	3/4[b]
55,713	2011 Jun 1	Minor flaring	20	59–62	4
55,715	2011 Jun 3	Minor flaring	40	77–80	4
55,716	2011 Jun 4	Minor flaring	20	70–74	4
55,717	2011 Jun 5	Minor flaring	20	79–81	4
55,720	2011 Jun 8	Minor flaring	20	76–78	4
55,721	2011 Jun 9	Minor flaring	10	74–75	4
55,733	2011 Jun 21	Minor flaring	14	45–48	4
55,734	2011 Jun 22	Minor flaring	10	64–68	4
55,735	2011 Jun 23	Minor flaring	46	59–69	4
55,736	2011 Jun 24	Minor flaring	84	74–80	4
55,737	2011 Jun 25	Minor flaring	40	69–73	4
55,738	2011 Jun 26	Quiescent	59.5	74–80	4
55,739	2011 Jun 27	Quiescent	95	71–80	4
55,740	2011 Jun 28	Quiescent	30	76–80	3
55,743	2011 Jul 1	Quiescent	20	76–80	4
55,744	2011 Jul 2	Quiescent	20	76–78	4
55,830	2011 Sep 26	Quiescent	80	78–80	3/4[b]
55,833	2011 Sep 29	Quiescent	48	74–80	4
55,834	2011 Sep 30	Quiescent	52	64–79	3/4[b]
55,835	2011 Oct 1	Quiescent	43.5	66–75	4
55,850	2011 Oct 16	Quiescent	28	74–80	4

Table 1
(Continued)

MJD	Calendar Date	X-Ray State	Observing Time (min)	Elevation Range (deg)	N_{tel}
55,851	2011 Oct 17	Quiescent	80	72–80	4
55,852	2011 Oct 18	Quiescent	71	68–80	4
55,853	2011 Oct 19	Quiescent	51	70–79	4
55,854	2011 Oct 20	Quiescent	111	70–79	4
55,855	2011 Oct 21	Quiescent	20	58–60	4
55,858	2011 Oct 24	Quiescent	20	59–61	4
55,860	2011 Oct 26	Quiescent	20	58–61	4
55,861	2011 Oct 27	Quiescent	17	70–74	4
55,862	2011 Oct 28	Quiescent	72	59–80	4
55,863	2011 Oct 29	Quiescent	35	74–80	4
55,864	2011 Oct 30	Quiescent	15	76–80	4
55,865	2011 Oct 31	Quiescent	40	66–76	4
55,888	2011 Nov 23	Quiescent	36	60–68	4
55,891	2011 Nov 26	Quiescent	20	61–64	4
55,892	2011 Nov 27	Quiescent	40	56–64	4
55,893	2011 Nov 28	Quiescent	20	52–56	4

Notes. The column N_{tel} shows the number of working telescopes.
[a] The hypersoft state consists of the data run contained within the quenched state. See text.
[b] One telescope was taken out of the operation during the run.

For background modeling, we included all of the sources in the Fermi Large Area Telescope Second Source (2FGL) Catalog (Nolan et al. 2012) that are in the vicinity of Cygnus X-3. To account for possible intrinsic variability of the sources, we allowed the spectral parameters of the sources in a 5° radius region of interest (RoI) to vary in an unbinned maximum likelihood analysis. On the other hand, we froze the spectral parameters of the sources that are outside of the RoI but within a 22° radius source region at the 2FGL values. To minimize contamination from a bright nearby pulsar, PSR J2032+4127 (about 30′ away from Cygnus X-3), following Corbel et al. (2012), we excluded the times of its peak-pulse emission, based on the pulsar ephemeris[35] (Ray et al. 2011). As for the Galactic and extragalactic diffuse gamma-ray backgrounds, we adopted the most recent models (*gal_2yearp7v6_v0.fits* and *iso_p7v6source.txt*). We also modeled the emission from the Cygnus Loop region with a template that is provided in the LAT Catalog Data Products. The instrument response function (IRF) used in this work is IRF P7SOURCE_V6.

We derived, from background modeling, the best-fit spectral parameters of the sources in the RoI. We then fixed the parameters for all other sources, as well as the spectral index of Cygnus X-3, and performed another unbinned maximum likelihood analysis, to produce a light curve of Cygnus X-3 over the time period of interest. The statistical significance of each measurement is quantified by a maximum likelihood test statistic (TS; Mattox et al. 1996), which corresponds roughly to $\sqrt{\mathrm{TS}}\,\sigma$ in Gaussian statistics.

3.2. X-Ray and Radio Observations

Contemporaneous X-ray coverages of Cygnus X-3 were provided by the All-sky Monitor (ASM) aboard the *RXTE* satellite (Levine et al. 1996), the Burst Alert Monitor (BAT) aboard the *Swift* satellite (Barthelmy et al. 2005), and the Monitor of All-sky X-ray Image (MAXI) aboard the International Space Station (Matsuoka et al. 2009). The ASM and MAXI cover soft X-ray bands of 1.5–12 keV and 2–20 keV, respectively, while the BAT covers the hard X-ray band of 15–50 keV. For this work, we chose to use the ASM and MAXI data in a narrower (soft) band, to achieve a more accurate characterization of the states (Szostek et al. 2008). We weighted the measured count rates or fluxes of Cygnus X-3 (by $1/\sigma^2$), which are made publicly available by the instrument teams and, if necessary, rebinned them to produce daily-averaged light curves.

At radio wavelengths, Cygnus X-3 is monitored regularly with the Arcminute Microkelvin Imager-Large Array (AMI-LA)[36] at the Mullard Radio Astronomy Observatory in the UK. The AMI-LA consists of eight 12.8 m Cassegrain antennas in a two-dimensional array, with a baseline of ∼120 m (Zwart et al. 2008). It operates in six frequency bands covering the range of 13.9–18.2 GHz. Here, we used the data taken from 2008 May 26 to 2011 December 31. Note that no data were taken between 2006 June 19 and 2008 May 26, due to the major upgrade of the Ryle Radio Telescope to the AMI-LA. The weighted, daily-averaged light curve was used for this work.

4. RESULTS

4.1. Blind Searches for TeV Gamma Rays

Using the full VERITAS data set, we found no significant ($>5\sigma$) excess of TeV gamma rays from Cygnus X-3 with the soft, medium, and hard data cuts. The significance was calculated with the modified Equation (17) of Li & Ma (1983), which is generalized for data sets with different source and background regions (Aharonian et al. 2004). The results are summarized in Table 2.

To derive a flux upper limit for each observing run, we calculated the total counts in the source region N_{on}, total counts in the background region N_{off}, and a scale factor α, which is defined as the ratio of the areas of the (geometrical or parameter) regions from which source and background counts are derived. The scale factor may be different for different cuts.

[35] The pulsar ephemeris for PSR J2032+4127 is available at http://www.slac.stanford.edu/∼abdo/LATPulsarTimingModels/Latest/J2032+4127/J2032+4127_latest.par.

[36] http://www.mrao.cam.ac.uk/∼guy/cx3/

Table 2
Results from Gamma-Ray Searches

Spectral State	Exposure Time (hr)	Elevation Range	On Events N_{on}	Off Events N_{off}	α_{eff}	Excess Events N_{ex}	Significance (σ)	Energy Threshold (GeV)	Flux Upper Limit (10^{-12} cm^{-2} s^{-1})
Soft Cuts									
All	44.70	42°–81°	17509	125799	0.136	400.3	0.6	182	5.0
Quiescent	23.04	52°–80°	9046	65596	0.136	124.9	0.3	182	4.6
Minor flaring	13.68	45°–81°	4032	28865	0.138	48.6	0.6	200	6.1
Suppressed	0.30	76°–78°	162	1069	0.156	−4.8	−0.4	200	64.6
Quenched	4.24	54°–81°	2410	16923	0.142	6.9	0.1	200	20.5
Hypersoft[a]	0.30	53°–63°	180	1360	0.142	−13.1	−0.9	316	29.0
Major flaring	3.44	42°–72°	1859	13344	0.138	17.5	0.4	316	10.9
Medium Cuts									
All	44.70	42°–81°	1200	26176	0.046	−4.1	−0.1	263	0.7
Quiescent	23.04	52°–80°	654	15268	0.046	−48.3	−1.7	263	0.5
Minor flaring	13.68	45°–81°	343	6813	0.046	29.6	1.5	288	2.1
Suppressed	0.30	76°–78°	11	94	0.047	6.6	2.5	288	41.8
Quenched	4.24	54°–81°	96	2097	0.047	−2.6	−0.1	347	2.5
Hypersoft[a]	0.30	53°–63°	8	205	0.045	−1.2	−0.4	457	9.0
Major flaring	3.44	42°–72°	96	1904	0.047	6.5	0.7	550	2.2
Hard Cuts									
All	44.70	42°–81°	145	3305	0.045	−3.7	−0.2	603	0.2
Quiescent	23.04	52°–80°	68	1936	0.045	−19.1	−2.0	603	0.1
Minor flaring	13.68	45°–81°	46	831	0.046	7.8	1.2	603	0.6
Suppressed	0.30	76°–78°	1	14	0.045	0.4	0.4	603	10.2
Quenched	4.24	54°–81°	13	281	0.046	0.1	0.0	871	0.9
Hypersoft[a]	0.30	53°–63°	3	25	0.042	2.0	1.5	871	9.2
Major flaring	3.44	42°–72°	17	244	0.047	5.5	1.5	955	1.2

Notes. Flux upper limits are given at the 95% C.L, and for each row are calculated from the energy threshold. The column α_{eff} shows the effective scale factor for the background calculation (see Section 4).

[a] The hypersoft state consists of the data run from 2008/12/04 (MJD 54804) and is a data run subset contained within the quenched state.

It may also vary from run to run, because, for instance, a bright star or known gamma source may need to be excluded from the background region in certain wobble configurations. For the analyses of multiple data runs, individual α values were weighted by corresponding background counts and averaged to produce an effective α_{eff} for the runs. To account for varying zenith angle conditions, an average effective area A_{eff} was constructed from individual effective areas for the runs. The flux upper limit was then derived from total N_{on}, total N_{off}, α_{eff}, A_{eff}, and total effective exposure time, with the method of Rolke et al. (2005).

Table 2 shows the 95% confidence level (C.L.) integral flux upper limits derived with the full VERITAS data set. We chose as the lower limit for flux integration the energy threshold, which is defined as the energy at which the differential rate of gamma-ray detection as a function of energy reaches its maximum. Different data cuts lead to different energy thresholds (also shown in the table). We should point out that we did not include systematic uncertainties in this or subsequent analyses.

4.1.1. Search for Episodic Emission

We also conducted a blind search for episodic TeV gamma-ray emission from Cygnus X-3. In this case, the VERITAS data runs were grouped on a night-by-night basis. As before, we selected events with the soft, medium, and hard cuts, respectively, and followed the same procedure to reduce and analyze the data. Figure 1 shows the distribution of the significance of excess for each set of cuts separately. The distributions are consistent with no significant TeV gamma-ray signal from Cygnus X-3 (with the 99% C.L. integral flux upper limits shown in the top panel of Figure 4 for individual nights).

4.1.2. Search for Orbital Modulation

Considering that gamma-ray production could be concentrated in certain parts of the binary orbit, we folded the data from all observing runs into 10 phase bins, using the ephemeris of Zdziarski et al. (2012). When a run spans multiple phase bins, we took care in dividing it so that the events fall in the correct bins. Again, we followed the same procedure to reduce and analyze the runs (or sub-runs) for each phase bin. We found no significant excess over the entire orbit. The 95% C.L. integral flux upper limits (derived with the medium cuts) are shown in Figure 2.

4.1.3. Spectral Constraints

To place constraints on the gamma-ray spectrum of Cygnus X-3 at TeV energies, we also analyzed the data for selected energy ranges. The 95% C.L. integral flux upper limits are given in Table 3, and the corresponding differential flux upper limits are shown in Figure 3. We adopted logarithmic energy binning ($\Delta E/E \sim 30\%$) for this analysis. The bins are coarser than the energy resolution of VERITAS but are sufficiently small to minimize any spectral dependence of the results. Such dependence may arise from the fact that the effective area is constructed, via Monte-Carlo simulations, with an assumed input spectrum (which, in this case, has a photon index of −2.4)

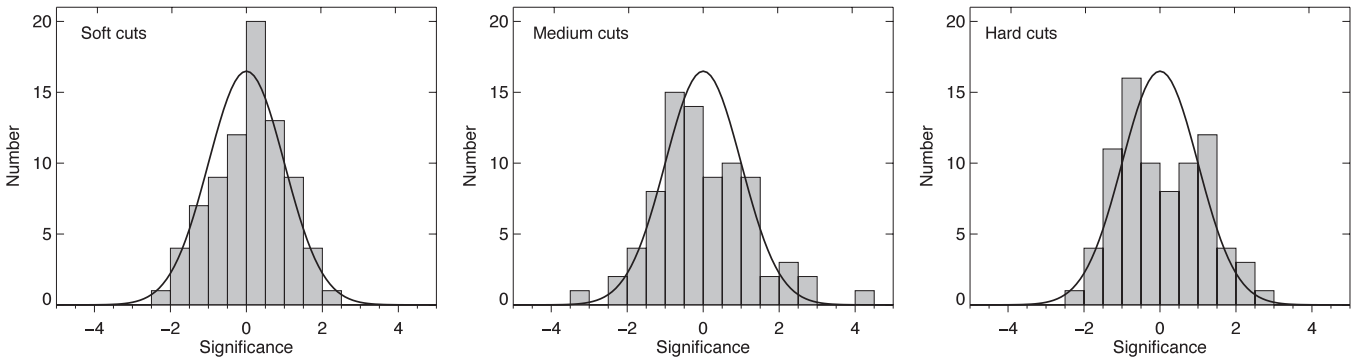

Figure 1. Gaussian significance (in units of σ) distributions for VERITAS nightly searches. The results from different data cuts are shown separately. The Gaussian functions with mean zero and σ one are shown in solid lines.

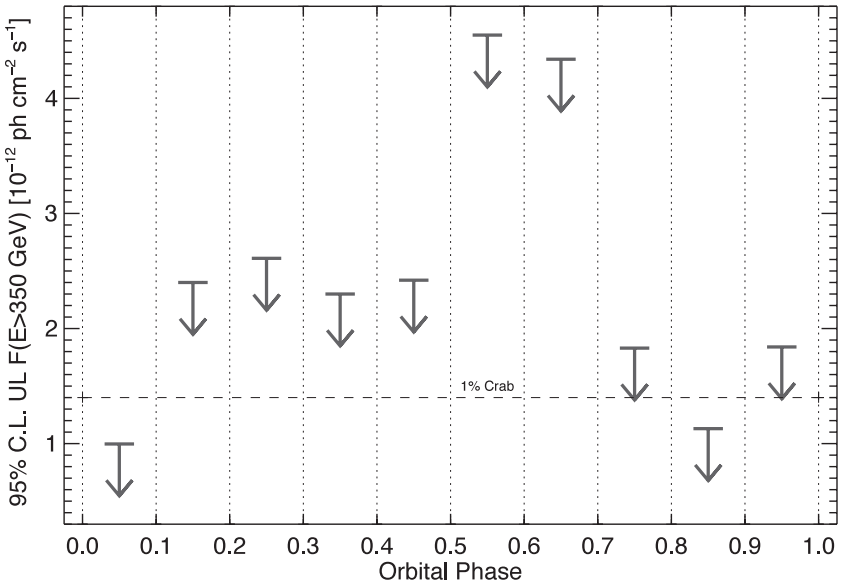

Figure 2. VERITAS phase-folded 95% C.L. integral ($E > 350$ GeV) flux upper limits of Cygnus X-3. For reference, the level of 1% Crab is indicated (in dashed line).

Table 3
Flux Upper Limits for Selected Energy Ranges

Energy Range (TeV)	On Events N_{on}	Off Events N_{off}	α_{eff}	Excess Events N_{ex}	Significance (σ)	Flux Upper Limit (10^{-12} cm^{-2} s^{-1})
0.263–0.342	230	4726	0.046	12.6	0.8	0.5
0.342–0.445	151	3801	0.046	−23.8	−1.9	0.1
0.445–0.578	126	2905	0.046	−7.6	−0.7	0.2
0.578–0.751	102	2229	0.046	−0.5	−0.1	0.2
0.751–0.977	65	1663	0.046	−11.5	−1.3	0.1
0.977–1.269	58	1253	0.046	0.4	0.0	0.2
1.269–1.650	36	1033	0.046	−11.5	−1.7	0.1
1.650–2.145	39	795	0.046	2.4	0.4	0.2
2.145–2.789	25	627	0.046	−3.8	−0.7	0.1
2.789–3.626	20	447	0.046	−0.6	−0.1	0.1
3.626–4.713	14	354	0.046	−2.3	−0.6	0.1

Note. As for Table 2, but for selected energy ranges.

and certain data cuts (which, in this case, are the medium cuts). Above about 5 TeV, the number of events that pass the cuts is so small that the results (not shown) become very uncertain. For comparison, we also plotted the published MAGIC differential flux upper limits (Aleksić et al. 2010) in the figure, as well as the extrapolation of the best-fit power-law spectra measured with *AGILE* and *Fermi* LAT.

4.2. Targeted Searches for TeV Gamma Rays in Radio/X-Ray States

As mentioned in Section 1, there appears to be evidence for gamma-ray production in Cygnus X-3 only in certain radio/X-ray states. For a more effective search, it is, therefore, important to characterize the states that the source is in.

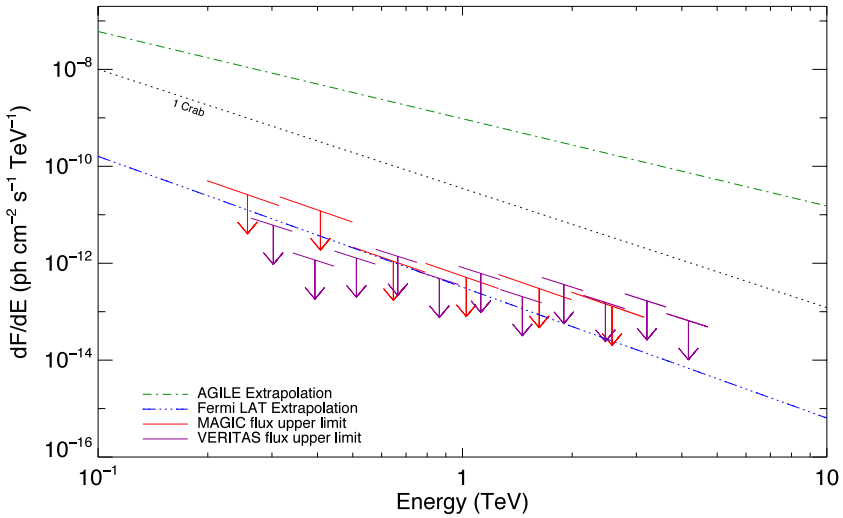

Figure 3. VERITAS 95% C.L. differential flux upper limits of Cygnus X-3. For comparison, the published MAGIC upper limits are shown in (red) thin solid lines. See Figure 1 and Table 2 of Aleksić et al. (2010) for further details concerning the MAGIC results. A nominal spectrum of the Crab Nebula is shown in the (black) dotted line, for reference. The (blue) dot-dot-dot-dashed line and (green) dot-dashed line show the extrapolations of the power-law spectra measured with the *Fermi* LAT and *AGILE* at GeV energies, respectively.

(A color version of this figure is available in the online journal.)

Fortunately, there were extensive X-ray and radio coverages of Cygnus X-3 that were contemporaneous with the VERITAS observations. We used the radio and (soft and hard) X-ray light curves of the source, as shown in Figure 4, to distinguish the states, as defined in Szostek et al. (2008). We chose to divide the post-flaring state appropriately and merge it into the minor flaring and suppressed states.

It is worth noting a few key features in the multi-wavelength light curves shown in Figure 4. First, the anti-correlation between the soft and hard X-ray bands is apparent, comparing the ASM/MAXI and *Swift* BAT light curves. Second, the quenched state is not easily recognizable based on the radio light curve alone. It is, in fact, more apparent in the hard X-ray light curves, as it is when hard X-ray emission is quenched as well. To be more quantitative, we define the quenched state as the time when the *Swift* BAT flux goes below 0.01 counts cm^{-2} s^{-1} (or when the ASM flux goes above 3 counts s^{-1}, as the soft/hard X-ray anti-correlation suggests). Finally, the times of significant detections of Cygnus X-3 at GeV energies (see the *Fermi*-LAT light curve) do seem to align with the transitions into or out of the quenched state (i.e., the hypersoft state) quite well.

We grouped the VERITAS observing runs based on the radio/X-ray states and carried out a search for TeV gamma rays from Cygnus X-3 for each of the states. The analysis was made with the soft, medium, and hard cuts. The results are shown separately in Table 2. No significant TeV gamma-ray signal was found in any of the searches.

5. DISCUSSION

The VERITAS observations of Cygnus X-3 covered the quenched state between 2008 October 30 and December 13 (MJD 54,769–54,813), when it was detected with *AGILE* (ATel 1827, Tavani et al. 2008b; and ATel 1848, Tavani et al. 2008a). Unfortunately, there was only one VERITAS observation in the hypersoft/quenched state on 2008 December 4. The source was not detected at TeV energies. The derived flux upper limits are not very constraining (see Table 2), due to limited VERITAS exposure.

The VERITAS observations also covered the major flaring state (reaching a peak radio flux of ∼20 Jy) that followed the 2011 March quenched state. Due to the low elevation of the source and other observing constraints, VERITAS missed the peak of the radio flare (on 2011 March 24 or MJD 55,644). The source was detected during this episode with the *Fermi* LAT (Corbel et al. 2012). The highest LAT flux occurred on 2011 March 22, just before the peak of the radio flare. We failed to detect a signal from the source at TeV energies over the period from 2011 March 28 to April 5.

Based on the entire VERITAS data set, we derived, with the medium cuts, a 95% C.L. integral flux upper limit of 0.7×10^{-12} photons cm^{-2} s^{-1} ($E > 263$ GeV), which is about a factor of three lower than the published MAGIC value ($E > 250$ GeV; Aleksić et al. 2010). Note that the difference in energy thresholds between the two measurements amounts only to an effect of a few percent. We have also made a direct comparison of the VERITAS and MAGIC constraints on differential fluxes at various energies (see Figure 3). Our upper limits are significantly lower than the MAGIC limits at lower energies. It should, however, be noted that we did not consider systematic uncertainties in our analyses, while the MAGIC results include a 30% systematic uncertainty on flux. The VERITAS flux upper limits are compatible with the results of spectral modeling carried out by Piano et al. (2012).

If we extrapolate the best-fit *Fermi* LAT spectrum of Cygnus X-3 (Abdo et al. 2009) to the VERITAS energy range, following a simple power law, we would expect an integral flux of $F(E > 263\ \mathrm{GeV}) = 1.8\times10^{-12}$ photons cm^{-2} s^{-1}, which is comparable to our 95% C.L. flux upper limit. However, the uncertainties on the *Fermi*-LAT spectrum make it difficult to conclude that a spectral break or rollover would be required from GeV to TeV energies. The episodic nature of the gamma-ray emission from Cygnus X-3 has made it even more difficult to compare *Fermi* LAT and VERITAS measurements. This is illustrated by the fact that the published *AGILE* spectrum of Cygnus X-3 (Tavani et al. 2009) is higher and harder than the *Fermi*-LAT spectrum. If we extrapolate the best-fit power law to the *AGILE* spectrum into the VERITAS energy range, we would

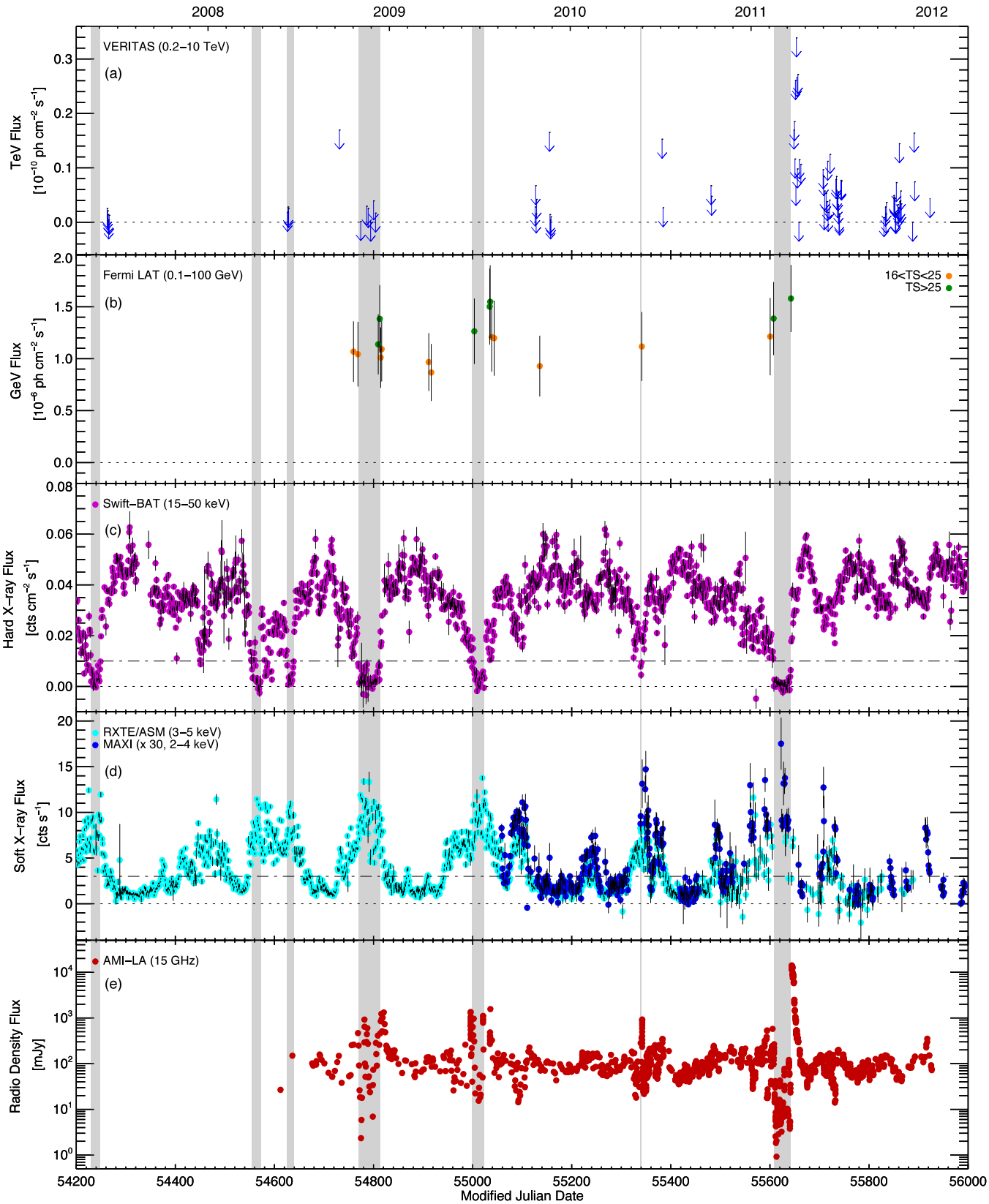

Figure 4. Multi-wavelength light curves of Cygnus X-3. Panels (a) TeV gamma ray. The VERITAS 99% C.L. integral ($E > 263$ GeV) flux upper limits are shown for individual nights. (b) GeV gamma ray. The data points are color-coded by the detection significance: moderate significance ($16 < \mathrm{TS} < 25$) in orange, and high significance ($\mathrm{TS} > 25$) in green. (c) Hard X-ray. (d) Soft X-ray. The ASM 3–5 keV measurements are shown in cyan and the MAXI 2–4 keV measurements in blue. Note that the MAXI flux values have been multiplied by 30 for clarity. (e) Radio. The AMI-LA 15 GHz measurements are shown. The shaded areas indicate the quenched state. The dot-dashed line in (c) and (d) shows roughly the threshold for transition into or out of the quenched state.

(A color version of this figure is available in the online journal.)

obtain an integral flux of $F(E > 263\,\mathrm{GeV}) = 3.5 \times 10^{-9}$ photons $\mathrm{cm}^{-2}\ \mathrm{s}^{-1}$ (with large uncertainties). More sophisticated spectral modeling is required to connect the *Fermi*-LAT and VERITAS data more physically (e.g., Piano et al. 2012), but it is beyond the scope of this work.

For microquasars, the kinetic power of the jets is of the order of $\sim 10^{38}$ erg s^{-1}, which is comparable to the bolometric luminosity of Cygnus X-3 (assuming a distance of 9 kpc; Hjalmarsdotter et al. 2008). Our flux upper limit corresponds to an upper limit on the TeV gamma-ray luminosity of $\approx 6 \times 10^{33}$ erg s^{-1}. This implies a maximum gamma-ray conversion efficiency of the order 10^{-4}–10^{-5}. In the context of leptonic models, Bednarek (2010) predicted a gamma-ray luminosity of $\approx 10^{32}$ erg s^{-1} for Cygnus X-3, assuming steady emission. This is discouraging for the current generation of ground-based gamma-ray facilities, although the episodic nature of GeV gamma-ray emission from the source argues for more patience. In our case, the most interesting radio/X-ray state (i.e., the hypersoft state) has hardly been covered (see Table 2). A concerted, multi-wavelength effort to target this state will likely be a more effective (and resource conserving) strategy for moving forward.

This work has made use of high-level data products provided by the ASM/*RXTE*, MAXI, and BAT/*Swift* teams. The AMI-LA radio results were obtained from a public archive maintained by Guy Pooley. Paul Ray is thanked for making available the ephemeris for PSR J2032+4127. A.V. and W.C. gratefully acknowledge financial support from NASA through a *Fermi* GI grant (NNX11AP90G) and from Purdue University. The VERITAS operation is supported by grants from the U.S. Department of Energy Office of Science, the U.S. National Science Foundation and the Smithsonian Institution, by NSERC in Canada, by Science Foundation Ireland (SFI 10/RFP/AST2748), and by STFC in the U.K. We acknowledge the excellent work of the technical support staff at the Fred Lawrence Whipple Observatory and at the collaborating institutions in the construction and operation of the instrument.

Facilities: VERITAS, Swift, RXTE, MAXI, Fermi, AGILE, AMI

REFERENCES

Abdo, A. A., Ackermann, M., Ajello, M., et al. (Fermi LAT Collaboration) 2009, Sci, 326, 1512
Acciari, V. A., Beilicke, M., Blaylock, G., et al. (VERITAS Collaboration) 2008, ApJ, 679, 1427
Aharonian, F., Akhperjanian, A., Beilicke, M., et al. 2004, A&A, 421, 529
Aharonian, F., Akhperjanian, A., Beilicke, M., et al. 2005, A&A, 431, 197
Aleksić, J., Antonelli, L. A., Antoranz, P., et al. 2010, ApJ, 721, 843
Atwood, W. B., Abdo, A. A., Ackermann, M., et al. 2009, ApJ, 697, 1071
Barthelmy, S. D., Barbier, L. M., Cummings, J. R., et al. 2005, SSRv, 120, 143
Bednarek, W. 2010, MNRAS, 406, 689
Bennett, K., Bignami, G., Hermsen, W., et al. 1977, A&A, 59, 273
Berge, D., Funk, S., & Hinton, J. 2007, A&A, 466, 1219
Borione, A., Chantell, M. C., Covault, C. E., et al. 1997, PhRvD, 55, 1714
Chardin, G., & Gerbier, G. 1989, A&A, 210, 52
Choudhury, M., Rao, A. R., Vadawale, S. V., Ishwara-Chandra, C. H., & Jain, A. K. 2002, A&A, 383, L35
Corbel, S., Dubus, G., Tomsick, J. A., et al. 2012, MNRAS, 421, 2947
Dubus, G., Cerutti, B., & Henri, G. 2010, MNRAS, 404, L55
Hillas, A. M. 1985, Proc. 19th Int. Cosmic Ray Conf., ed. F. C. Jones (Washington, DC: NASA), 3, 445
Hjalmarsdotter, L., Zdziarski, A. A., Larsson, S., et al. 2008, MNRAS, 384, 278
Holder, J., Aliu, E., Arlen, T., et al. 2011, Proc. 32nd Int. Cosmic Ray Conf. (Beijing), 12, 137 (arXiv:1111.1225)
Koljonen, K. I. I., Hannikainen, D. C., McCollough, M. L., Pooley, G. G., & Trushkin, S. A. 2010, MNRAS, 406, 307
Krawczynski, H., Carter-Lewis, D. A., Duke, C., et al. 2006, APh, 25, 380
Lamb, R. C., Fichtel, C. E., Hartman, R. C., Kniffen, D. A., & Thompson, D. J. 1977, ApJL, 212, L63
Levine, A. M., Bradt, H., Cui, W., et al. 1996, ApJL, 469, L33
Li, T. P., & Ma, Y. Q. 1983, ApJ, 272, 317
Ling, Z., Zhang, S. N., & Tang, S. 2009, ApJ, 695, 1111
Matsuoka, M., Kawasaki, K., Ueno, S., et al. 2009, PASJ, 61, 999
Mattox, J. R., Bertsch, D. L., Chiang, J., et al. 1996, ApJ, 461, 396
McCollough, M. L., Robinson, C. R., Zhang, S. N., et al. 1999, ApJ, 517, 951
Miller-Jones, J. C. A., Blundell, K. M., Rupen, M. P., et al. 2004, ApJ, 600, 368
Mioduszewski, A. J., Rupen, M. P., Hjellming, R. M., Pooley, G. G., & Waltman, E. B. 2001, ApJ, 553, 766
Mori, M., Bertsch, D. L., Dingus, B. L., et al. 1997, ApJ, 476, 842
Nolan, P. L., Abdo, A. A., Ackermann, M., et al. 2012, ApJS, 199, 31
O'Flaherty, K. S., Cawley, M. F., Fegan, D. J., et al. 1992, ApJ, 396, 674
Ong, R. A. 1998, PhR, 305, 93
Piano, G., Tavani, M., Vittorini, V., et al. 2012, A&A, 545, A110
Predehl, P., Burwitz, V., Paerels, F., & Trümper, J. 2000, A&A, 357, L25
Ray, P. S., Kerr, M., Parent, D., et al. 2011, ApJS, 194, 17
Rolke, W. A., López, A. M., & Conrad, J. 2005, NIMPA, 551, 493
Romero, G. E., Torres, D. F., Kaufman Bernadó, M. M., & Mirabel, I. F. 2003, A&A, 410, L1
Schilling, M., Mang, O., & Siems, M. 2001, Proc. 27th Int. Cosmic Ray Cong. (Hamburg), 6, 2521
Szostek, A., Zdziarski, A. A., & McCollough, M. L. 2008, MNRAS, 388, 1001
Tavani, M., Bulgarelli, A., Piano, G., et al. 2009, Natur, 462, 620
Tavani, M., Piano, G., Chen, A., et al. 2008a, ATel, 1848, 1
Tavani, M., Sabatini, S., Piano, G., et al. 2008b, ATel, 1827, 1
van Kerkwijk, M. H., Geballe, T. R., King, D. L., van der Klis, M., & van Paradijs, J. 1996, A&A, 314, 521
Waltman, E. B., Fiedler, R. L., Johnston, K. L., & Ghigo, F. D. 1994, AJ, 108, 179
Weekes, T. C. 1992, SSRv, 59, 315
Zdziarski, A. A., Maitra, C., Frankowski, A., Skinner, G. K., & Misra, R. 2012, MNRAS, 426, 1031
Zwart, J. T. L., Barker, R. W., Biddulph, P., et al. 2008, MNRAS, 391, 1545